Sunlight-Fueled, Low-Temperature Ru-Catalyzed Conversion of CO_2 and H_2 to CH_4 with a High Photon-to-Methane Efficiency

Francesc Sastre,[†] Caroline Versluis,[†] Nicole Meulendijks,[†] Jessica Rodríguez-Fernández,[†] Jorgen Sweelssen,[†] Ken Elen,[‡,§] Marlies K. Van Bael,[‡,§] Tim den Hartog,[†,‖] Marcel A. Verheijen,[⊥,#] and Pascal Buskens[*,†,‡,‖]

[†]The Netherlands Organisation for Applied Scientific Research (TNO), High Tech Campus 25, 5656AE Eindhoven, The Netherlands

[‡]Institute for Materials Research, Inorganic and Physical Chemistry, Hasselt University, Agoralaan Building D, B-3590 Diepenbeek, Belgium

[§]IMEC vzw, IMOMEC Associated Laboratory, Wetenschapspark 1, B-3590 Diepenbeek, Belgium

[‖]Zuyd University of Applied Sciences, Nieuw Eyckholt 300, 6400AN Heerlen, The Netherlands

[⊥]Philips Innovation Labs, High Tech Campus 11, 5656AE Eindhoven, The Netherlands

[#]Department of Applied Physics, Eindhoven University of Technology, 5600MB Eindhoven, The Netherlands

S Supporting Information

ABSTRACT: Methane, which has a high energy storage density and is safely stored and transported in our existing infrastructure, can be produced through conversion of the undesired energy carrier H_2 with CO_2. Methane production with standard transition-metal catalysts requires high-temperature activation (300−500 °C). Alternatively, semiconductor metal oxide photocatalysts can be used, but they require high-intensity UV light. Here, we report a Ru metal catalyst that facilitates methanation below 250 °C using sunlight as an energy source. Although at low solar intensity (1 sun) the activity of the Ru catalyst is mainly attributed to thermal effects, we identified a large nonthermal contribution at slightly elevated intensities (5.7 and 8.5 sun) resulting in a high photon-to-methane efficiency of up to 55% over the whole solar spectrum. We attribute the excellent sunlight-harvesting ability of the catalyst and the high photon-to-methane efficiency to its UV−vis−NIR plasmonic absorption. Our highly efficient conversion of H_2 to methane is a promising technology to simultaneously accelerate the energy transition and reduce CO_2 emissions.
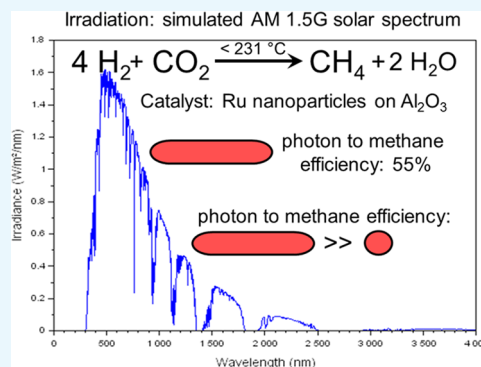
INTRODUCTION

To secure our future energy supply,[1] it will be necessary to build up storage capacities for extremely large amounts of energy. Such storage buffers are required for temporal matching of demand and supply as the energy generated from renewable sources,[2] e.g., solar and wind, inherently fluctuates. To limit land use, energy should be stored in materials with a high gravimetric storage density, i.e., chemical bonds.[3] Hydrogen[4] (H_2) seems attractive due to its high gravimetric storage density and the mature technology for its production through electrolysis. However, large-scale application of H_2 is problematic due to safety issues associated with large quantity storage, incompatibility with current gas distribution infrastructure, and high costs to construct or upgrade infrastructure. By transforming the H−H bond from green H_2 into C−H bonds of methane (CH_4),[5] it is possible to produce a green energy carrier with high gravimetric storage density that is actually currently used in our infrastructure. Carbon dioxide (CO_2) serves as a carbon source for this

methanation and, therefore, this process can help to reduce CO_2 emitted from point sources.

For this methanation to be sustainable as a whole, it is necessary that all energy required to drive the process directly originates from sunlight, i.e., no transformation of light into electricity (which inherently leads to energy losses) is needed. This process would require improvements over the current state-of-the-art Sabatier process,[6] which requires high temperatures (300−500 °C), and the use of semiconductor photocatalysts,[7] which can harvest only the short wavelength part of the solar spectrum and would thus require highly concentrated UV light (Figure 1).

Plasmonic nanomaterials, e.g., metallic nanoparticles of Au, Ag, and Al, can transform light into heat and hot charge carriers,[8] which opens up multiple pathways for promoting
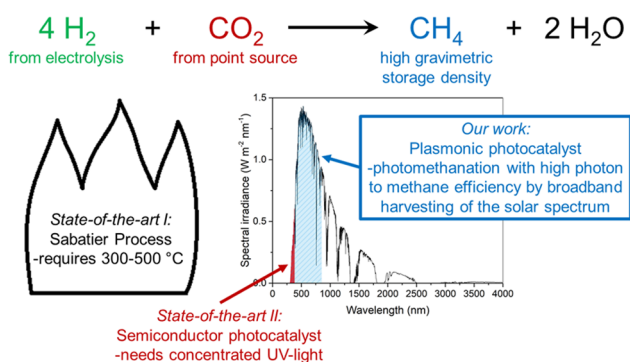
Figure 1. State-of-the-art methanation, and our low-temperature photomethanation reaction with broad-band absorption of sunlight.

catalytic processes. Photoinduced increase of the temperature of plasmonic nanoparticle catalysts may provide heat to nearby reactants, resulting, e.g., in increased reaction rates. Alternatively, hot electrons may be generated and transferred to a reactant in close proximity to the particle surface, which can influence, e.g., rate or selectivity of catalytic processes. Third, the photon rate seen by adjacent reactants may be increased because of enhancement of the optical nearfield adjacent to the nanoparticle. A recent review by Baffou and Quidant provides an overview of the main mechanisms involved in plasmon catalysis.[8] Depending on their type of metal, size, and shape, they can harvest a particular part of the sunlight spectrum.[9] Combining plasmonic nanoparticles with several sizes and shapes within a single catalyst could be exploited to harvest the energy from the entire solar spectrum reaching the earth's surface. Recently, Corma, García, and co-workers[10] used a combination of a metallic and a semiconductor catalyst, i.e., Ni and NiO nanoparticles, for photomethanation with concentrated light at 150 °C. This study does not differentiate between the contribution of the metallic and semiconductor

catalyst and is not carried out with terrestrial sunlight. Ye and co-workers[11] screened a variety of group VIIIb nanoparticles, including Ru and Rh, for photomethanation using highly concentrated light to heat the catalyst to approximately 300 °C (bulk photothermal heating) for carrying out the state-of-art Sabatier process. Liu and co-workers proposed a technique to distinguish between thermal and nonthermal contributions in plasmon catalysis.[12] For photomethanation of CO_2 using titania-supported Rh nanospheres as a catalyst, they determined an apparent quantum efficiency of 46% for high-intensity UV light ($\lambda = 365$ nm, photon flux $\Phi = 2.7$ W cm^{-2}) and a catalyst temperature of 350 °C. To the best of our knowledge, this is the highest reported apparent quantum efficiency to date for plasmon-catalyzed photomethanation of CO_2. An extensive overview of the literature on photomethanation processes with correspondingly reported catalytic activities has been added to the Supporting Information (SI, Table S1). Furthermore, Liu and co-workers demonstrated that illumination of Rh nanoparticle catalysts with UV light can be applied to tune the selectivity in the catalytic hydrogenation of CO_2, toward either CH_4 or CO.[13]

Here, we report a rod-shaped Ru metal catalyst on Al_2O_3 that facilitates photomethanation. We managed to promote the methanation using sunlight as a sole energy source. Furthermore, we demonstrate a large nonthermal contribution of sunlight to the reaction, resulting in a high photon-to-methane (PTM) efficiency of up to 55%. We attribute the excellent sunlight-harvesting ability of our catalyst and the high photon-to-methane efficiency to its plasmon resonance in the UV−vis−NIR, which relates to the geometry of the catalyst and, thus, provides valuable guidelines for catalyst design. Our highly efficient conversion of H_2 to methane is a promising technology to simultaneously accelerate the energy transition and reduce CO_2 emissions.
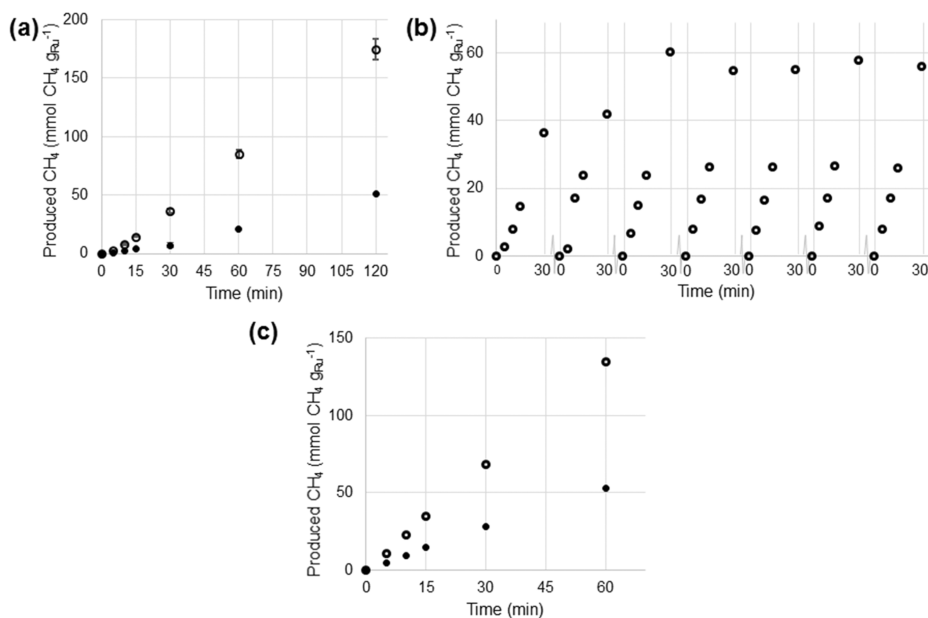

Figure 2. (a) Solar methanation (o) vs methanation in dark (●) using a nonactivated catalyst, (b) seven sequential solar methanation runs using a nonactivated catalyst, and (c) solar methanation (○) vs methanation in dark (●) using an activated catalyst. Reaction conditions: reaction mixture of $H_2/CO_2/N_2$ (5:1:1) at 3.5 bar pressure, 300 mg of either RuO_2 precatalyst or the preactivated Ru catalyst, reactor temperature 150 °C, 1 sun (or 0 sun) light intensity.
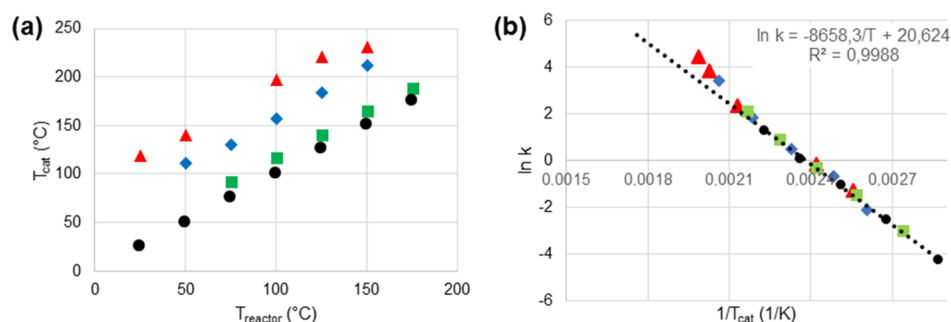
Figure 3. (a) Measured catalyst temperatures upon illumination (●: 0 sun; green box solid: 1 sun; blue diamond solid: 5.7 sun; red triangle up solid: 8.5 sun) and (b) Arrhenius plot displaying observed reaction rates for the methanation at various reactor temperatures and light intensities (●: 0 sun; green box solid: 1 sun; blue diamond solid: 5.7 sun; red triangle up solid: 8.5 sun). Reaction conditions: reaction mixture of $H_2/CO_2/N_2$ (5:1:1) at 3.5 bar pressure, 300 mg of the preactivated Ru catalyst, reactor temperatures: 25, 50, 75, 100, 125, 150 or 175 °C; light intensities: dark, 1, 5.7 or 8.5 sun.

■ RESULTS AND DISCUSSION

In search of a catalyst that consists of plasmonic metallic particles with a variety of shapes and sizes so that it can harvest a large part of the solar energy, we prepared RuO_2 nanocrystals supported on γ-Al_2O_3 (6.0 wt % Ru) via a wet impregnation technique (Experimental Section). This material was used as a precatalyst for the methanation at 1 sun light intensity (1 kW m^{-2}) and 150 °C reactor temperature (Experimental Section), which leads only to formation of CH_4 and H_2O as products. After 2 h, 174 ± 9 mmol CH_4 g_{Ru}^{-1} was obtained under these conditions, whereas only a fraction of this amount (51 mmol CH_4 g_{Ru}^{-1}) was produced without illumination at the same reactor temperature. Thus, the catalyst is substantially more active under illumination with terrestrial sunlight when compared to dark.

To investigate the stability of the catalyst under reaction conditions, we used the catalyst in seven sequential 30 min reactions at 1 sun and 150 °C (Figure 2b). Reproducibly, the first two runs gave a lower yield of methane (first run 36 ± 2 mmol CH_4 g_{Ru}^{-1}) than the runs 3–7 (57 ± 2 mmol CH_4 g_{Ru}^{-1}), indicating that the RuO_2 precatalyst is reduced in situ to the metallic Ru catalyst during the first reaction runs. No catalyst deactivation was observed from the third to the seventh run. Preactivation of the RuO_2 precatalyst with H_2 for 2 h at 250 °C allowed us to obtain a more active Ru catalyst. Use of this catalyst for the methanation reaction at 150 °C and 1 sun illumination resulted in a 1.6-fold increase in yield after a 1 h reaction time (135 mmol CH_4 g_{Ru}^{-1}, Figure 2c) versus the use of the RuO_2 precatalyst (85 mmol CH_4 g_{Ru}^{-1}, Figure 2a). Again, only a fraction of methane was produced without illumination at the same reactor temperature (53 mmol CH_4 g_{Ru}^{-1} in 1 h, Figure 2c).

To differentiate between thermal and nonthermal effects contributing to the sunlight-fueled methanation, we performed kinetic studies using the activated Ru catalyst and different combinations of reactor temperature (between 25 and 190 °C) and sunlight intensity (dark, 1, 5.7, 8.5 sun). In all experiments, the catalyst temperature was monitored by placing a thermocouple directly under the catalyst bed (SI, Figure S3). In a comparative experiment using an infrared camera, we confirmed the correctness of the catalyst temperature determined with the thermocouple (SI, Figure S6). As depicted in Figure 3a, the catalyst temperature increases substantially upon illumination.

For the experiment performed at $T_{reactor}$ = 150 °C and 1 sun solar intensity, the catalyst temperature T_{cat} increased to 164 °C. Higher solar intensities resulted in a further increase in the catalyst temperature, with a maximum of 231 °C obtained for $T_{reactor}$ = 150 °C and 8.5 sun. To differentiate between thermal and nonthermal contributions of sunlight illumination, we studied the reaction kinetics for different combinations of reactor temperature ($T_{reactor}$ between 25 and 190 °C) and sunlight intensity (dark, 1, 5.7, 8.5 sun) and compared the reaction rates to those obtained in dark at the same catalyst temperature. The results of this study are depicted in the Arrhenius plot (Figure 3b). The results clearly demonstrate that at the standard solar intensity of 1 sun and catalyst temperatures up to 189 °C the contribution of illumination with sunlight is largely thermal since the obtained reaction rates are nearly identical to those obtained in dark for the same catalyst temperature. At solar intensities of 5.7 and 8.5 sun, the contribution is largely thermal up to a catalyst temperature of approximately 200 °C. At higher catalyst temperatures of 212 °C ($T_{reactor}$ = 150 °C + 5.7 sun), 221 °C ($T_{reactor}$ = 125 °C + 8.5 sun), and 231 °C ($T_{reactor}$ = 150 °C + 8.5 sun), respectively, the reaction rates are 1.93, 2.12, and 2.73 times higher than the calculated rate obtained in dark at the same catalyst temperature. From the kinetics study, we calculated a photon-to-methane (PTM) efficiency to quantify the nonthermal contribution of solar illumination as follows

$$PTM = 100\% \frac{k_l - k_d}{\Phi A}$$

with k_l = reaction rate upon illumination, k_d = reaction rate in dark at the same catalyst temperature as in the illumination reaction, Φ = photon flux, and A = illuminated area. This PTM carries the same definition as the apparent quantum efficiency introduced by Liu and co-workers.[12] Both terms represent the ratio of the nonthermal share of the reaction rate to the rate of incident photons, and reported values are therefore directly comparable. We decided to introduce the term "photon-to-methane efficiency" because it accurately represents the efficiency of solar methanation reactions as the ratio of CH_4 molecules produced to incident photons. We consider the term "quantum efficiency" confusing in this respect since it is defined as the ratio of photocurrent versus the rate of incident photons to characterize optoelectronic devices. Hence, it describes the share of energy from (sun)light that is converted to electrical energy. In the Sabatier process, solar energy is not converted to chemical energy since the reaction is exothermic.
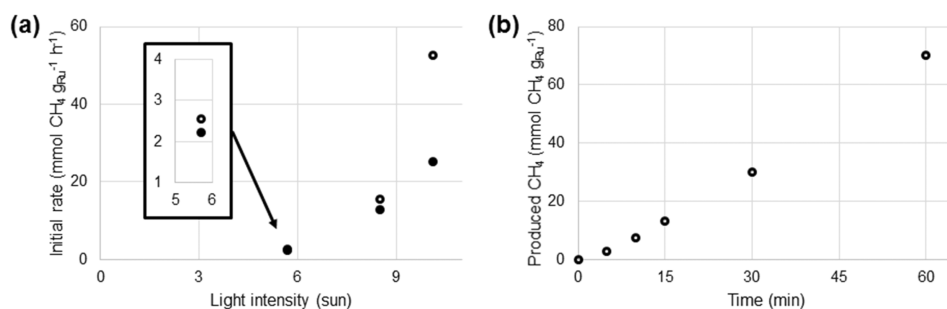
Figure 4. Photomethanation at $T_{reactor}$ = 25 °C: (a) initial rates for the production of methane as a function of light intensity (○) compared to initial rates in dark at the same catalyst temperature (●), and (b) produced amount of CH_4 g_{Ru}^{-1} using the preactivated Ru catalyst at 10.1 sun light intensity as a function of reaction time. Reaction conditions: reaction mixture of $H_2/CO_2/N_2$ (5:1:1) at 3.5 bar pressure, 300 mg preactivated Ru catalyst, 25 °C under the illumination of 5.7, 8.5, or 10.1 sun light intensity. Initial rates upon illumination were determined using multiple data points acquired in the first 15 min of the reaction; initial rates in dark were calculated according to the Arrhenius plot in Figure 3b.

The PTMs obtained for the reactions at $T_{reactor}$ = 150 °C + 5.7 sun (T_{cat} = 212 °C), $T_{reactor}$ = 125 °C + 8.5 sun (T_{cat} = 221 °C), and $T_{reactor}$ = 150 °C + 8.5 sun (T_{cat} = 231 °C), respectively, are 22.3, 25.0, and 54.8%. Compared to the best PTM reported for photomethanation of CO_2 by Liu and co-workers,[12] we realized a substantially higher PTM (54.8 vs 46%) at lower temperature (231 vs 350 °C), lower light intensity (0.85 vs 2.7 W cm^{-2}), and for broad-spectrum sunlight rather than for monochromatic UV light of a wavelength of 365 nm.

In addition to the high PTM achieved in this process, we have demonstrated that conventional heating of the reactor is not required to promote the methanation (Figure 4). At a solar intensity of 8.5 sun and $T_{reactor}$ = 25 °C, the reaction proceeded with a rate of 15.5 mmol CH_4 g_{Ru}^{-1} h^{-1} (Figure 4a). At 25 °C and 10.1 sun, the photomethanation rate (52 mmol CH_4 g_{Ru}^{-1} h^{-1}) was approximately 18 times higher than the previously reported[7h] 2.8 mmol CH_4 g_{Ru/SiO_2}^{-1} h^{-1} for $T_{reactor}$ = 25 °C and 24.7 sun (Figure 4b). Furthermore, for all sunlight intensities (5.7, 8.5, and 10.1 sun), the obtained reaction rates were higher than for the dark reaction (calculated values based on the Arrhenius plot in Figure 3b), demonstrating a nonthermal contribution to the reaction rate. The nonthermal contribution to the reaction rate increases with increasing solar intensity.

To gain insight into this highly efficient photomethanation, we studied the RuO_2 precatalyst (SI, S12 and S14) and the activated Ru catalyst with transmission electron microscopy (TEM, Figure 5a–j), X-ray diffraction analysis (XRD, Figure 5k), and X-ray photoelectron spectroscopy (SI, S16). These studies confirm that the RuO_2 precatalyst, which consists of single crystalline nanorods and has the orthorhombic RuO_2 structure (SI, Figure S14), is transformed into the activated Ru catalyst by solid-state recrystallization toward metallic Ru. This is performed either under typical reaction conditions or upon reduction with H_2 (preactivated catalyst). TEM confirms that the anisotropic shape of the RuO_2 nanoparticles is largely retained in the activated Ru catalyst. However, the recrystallization process is initiated by many separate nucleation events of the metallic phase, leading to polycrystalline Ru rods, as confirmed by the selected area electron diffraction (SAED) pattern in Figure 5j.

Analysis of Ru on the Al_2O_3 catalyst (obtained through reduction under typical reaction conditions) by bright-field (BF)TEM and high-angle annular dark-field scanning transmission electron microscopy (HAADF-STEM) (Figure 5a,b, respectively) and energy-dispersive X-ray spectroscopy (EDX)
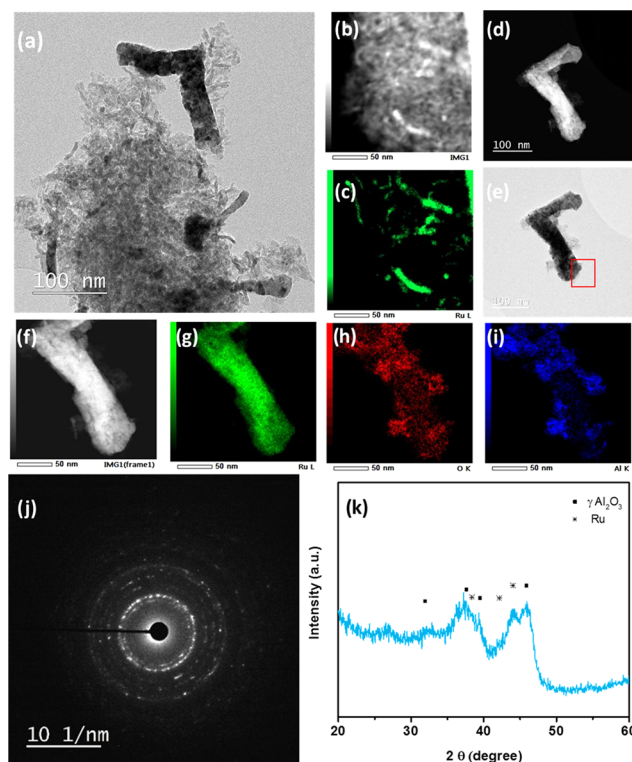

Figure 5. TEM and XRD analyses of the Ru catalyst: (a) bright-field TEM (BF-TEM) image of Ru on Al_2O_3; (b) high-angle annular dark-field scanning transmission electron microscopy (HAADF-STEM) of Ru on Al_2O_3; (c) energy-dispersive X-ray spectroscopy (EDX) mappings of Ru of (b); (d) HAADF-STEM image of two Ru crystals, decorated by a few Al_2O_3 particles; (e) BF-TEM image of two Ru crystals, decorated by a few Al_2O_3 particles; (f) higher magnification of (d); (g–i) EDX mappings of Ru (g), O (h), and Al (i) for (f); (j) selected area electron diffraction pattern, acquired from the area indicated in (e); (k) XRD pattern of the activated Ru catalyst supported on γ-Al_2O_3.

mapping of Ru in the HAADF sample (Figure 5c) shows that Ru nanostructures are present in a variety of shapes, among others nanospheres and (anisotropic) nanorods, with a variety of sizes. Studying several samples, we determined that the average diameter of the nanospheres was 11 ± 4 nm and that the average length and width of the nanorods were 153 ± 45 and 11 ± 10 nm, respectively (TEM analysis, SI, S17). A representative, detailed TEM study of two Ru nanocrystals supported on a few Al_2O_3 crystals found in our catalyst is

displayed in Figure 5d−j. HAADF-STEM and EDX-mapping of the elements Ru, O, and Al (Figure 5f−i) proved the metallic nature of the nanorods. BF-TEM (Figure 5e) and HAADF-STEM (Figure 5d) imaging allowed us to determine that the Ru nanorods are polycrystalline. This is further evidenced by the presence of rings in the SAED pattern in Figure 5j. Finally, the crystallinity of the catalyst is confirmed by XRD analysis (Figure 5k), giving reflections for the metallic Ru located at 2θ = 38.39 and 44.01°. From Scherrer analysis of the peak width in the XRD patterns, we obtained an average grain size of 11 nm. This is in agreement with the dimensions of the polycrystalline domains in the nanorods as well as with the average diameter of the nanospheres.

To gain insight into the sunlight absorption properties of the Ru catalyst, we determined the UV−vis−NIR diffuse reflectance of a powder sample. The $(100 - R)$ spectrum of the KBr-diluted powder, which is directly related to its absorption, is displayed in Figure 6a. The spectrum clearly
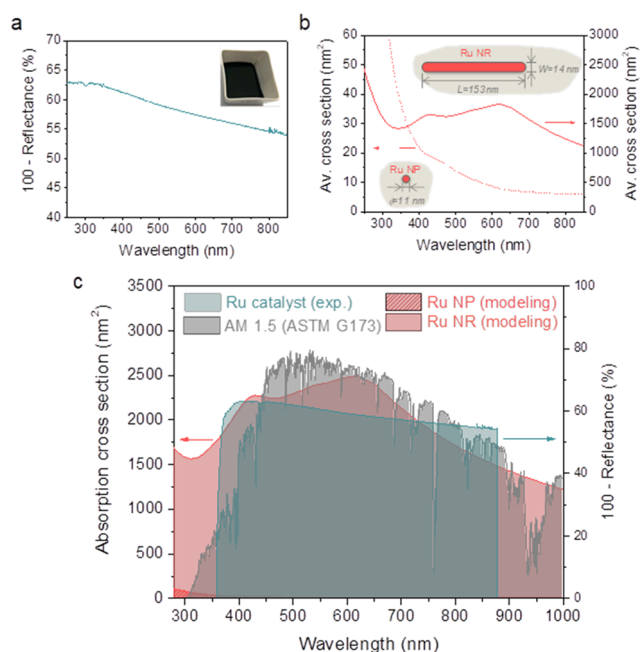

Figure 6. Optical characterization and modeling of the Ru catalyst: (a) $(100 - R)$ UV−vis−NIR spectrum of the Ru catalyst (inset: representative photograph of the γ-Al$_2$O$_3$ supported Ru catalyst), (b) calculated UV−vis−NIR extinction cross section of a single spherical Ru nanoparticle (11 nm diameter, dashed curve) and of a single Ru nanorod (length × width = 153 nm × 14 nm, aspect ratio = 10.9, solid curve) embedded in a γ-Al$_2$O$_3$ medium (inset: scale depiction of both nanoparticle types), and (c) solar spectrum coverage of our experimental Ru catalyst (blue), of the modeled single spherical Ru nanoparticle (11 nm, red patterned filling), and of the modeled Ru nanorod (153 nm × 14 nm, red, nonpatterned, filling) as compared to the AM 1.5 (ASTM G173) solar spectrum used in our work for sunlight-fueled CO$_2$ methanation (gray). Note that, for the sake of clarity, the y-axis scale of the AM 1.5 spectrum (0−1.8 W m^{-2} nm^{-1}) is not shown.

shows that the Ru catalyst features a broad and asymmetric absorption, which spans the UV−vis−NIR range with a maximum at ~310 nm. Given the large size and shape polydispersity of the Ru nanoparticles present in our Ru catalyst sample, it is important to disentangle their relative contribution to the catalyst's UV−vis−NIR light absorption

properties. For this purpose, we performed optical simulations based on the boundary element method[14] (BEM, SI, S21 for details) to determine the extinction spectra of the two most representative nanoparticle geometries present in our catalyst sample: spherical Ru nanoparticles [diameter (ϕ) = 11 nm, SI, S17 for details] and Ru nanorods (length × width = 153 nm × 14 nm, SI, S17 for details). Based on the previous work performed on polycrystalline Au nanorods and nanoshells, we anticipate that the polycrystallinity of the Ru nanorods will not significantly influence its plasmonic properties.[15] Figure 6b shows the calculated averaged cross sections (comparable to the extinction cross sections) in the 250−850 nm wavelength range (full range spectra in SI, Figure S28) of those individual nanoparticles dispersed in a γ-Al$_2$O$_3$ medium [which is the actual catalyst support, $n(\gamma$-Al$_2$O$_3) \sim 1.766$ at 2.059 eV].[16] The calculated spectra resemble closely the experimental spectral response of the Ru catalyst shown in Figure 6a. The calculated spectrum of the spherical Ru nanoparticle is characterized by a steep extinction for $\lambda < 400$ nm, which coincides with the onset of its characteristic UV plasmon band[17] (centered at ~205 nm, SI, Figure S28a), by a weak shoulder at ~445 nm, and by an essentially featureless, and nonzero, extinction for $\lambda > 600$ nm. The Ru nanorod also features a steep extinction for $\lambda < 340$ nm (its characteristic UV plasmon band is centered at ~184 nm, SI, Figure S28b). However, differently from the spherical Ru nanoparticle, it features a significant extinction in the vis−NIR range resulting from a broad and symmetric band centered at ~620 nm and from a (weaker) band peaking at ~430 nm. Optical simulations performed at different angles of light incidence (SI, Figure S29) indicate that the nanorod's vis−NIR plasmon bands at ~430 and ~620 nm occur only when the angle of light incidence is $\neq 0°$ with respect to its longitudinal axis, i.e., when its longitudinal plasmon modes are being excited. On the other hand, the excitation of the nanorod's UV plasmon band at ~184 nm (~2-fold more intense than the vis−NIR ones) occurs mainly upon illumination at 0° light incidence, i.e., upon transverse plasmon mode excitation. Given the large size of the Ru nanorod considered herein, it is likely that the nanorods may accommodate not only dipolar plasmon resonances but also higher order plasmon modes, as previously reported for other metal nanoparticles of comparable dimensions.[18] An accurate plasmon mode assignment for both the UV and vis−NIR plasmon bands of the Ru nanorod would therefore require a thorough optical modeling investigation that goes beyond the scope of this work.

In any case, our optical modeling results indicate that nonspherical, anisotropic Ru nanoparticles, such as the large and high aspect ratio Ru nanorods present in our catalyst sample, feature not only a characteristic plasmon band in the UV but also plasmon bands that span the visible and NIR range. Given that light absorption governs the overall contribution to light extinction for both nanoparticle types (SI, Figure S30), it can be concluded that the broad-band absorption of our γ-Al$_2$O$_3$-supported Ru catalyst (Figure 6a) is the result of all plasmon band contributions from the randomly distributed spherical and nonspherical Ru nanoparticles of various sizes present in our catalyst sample and from the plasmon coupling effects that may arise as a result of their sometimes small interparticle separation distances.[19] Importantly, our results demonstrate that a catalyst comprising solely Ru nanorods such as the ones presented in this study features a plasmonic absorption profile that matches that of the terrestrial
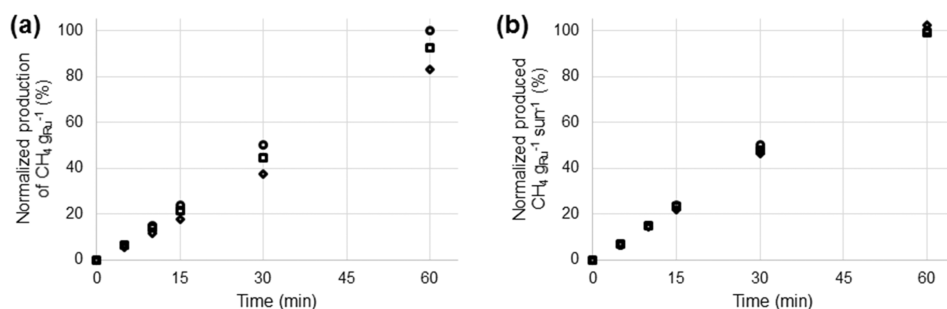
Figure 7. Effect of selective sunlight cutoff on the Ru catalyst's photomethanation performance: (a) produced amount of methane g_{Ru}^{-1} using H_2-activated Ru catalyst under 1 sun illumination without filter (O), with a filter that cuts off all light with a wavelength shorter than 395 nm (□), and 495 nm (◇) as a function of reaction time, and (b) produced amount of methane g_{Ru}^{-1} sun^{-1} as a function of reaction time for the above-mentioned cutoff filters. Reaction conditions: reaction mixture of $H_2/CO_2/N_2$ (5:1:1) at 3.5 bar total pressure, 300 mg H_2-activated Ru catalyst, 150 °C, either 1, 0.93, or 0.81 sun light intensity.
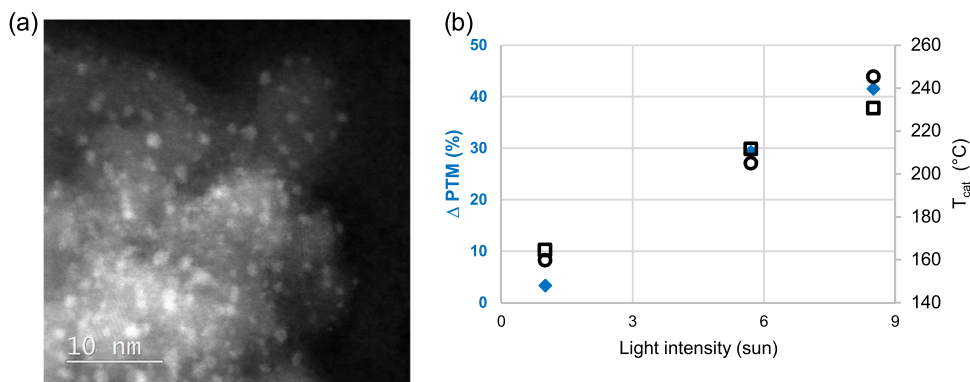

Figure 8. (a) HAADF-STEM image of the spherical Ru catalyst, and (b) reactivity and comparison of photon-to-methane efficiency and T_{cat} using rodlike vs spherical Ru-catalysts. The difference in PTM′ obtained with Ru rods−Ru spheres at $T_{reactor}$ = 150 °C (blue diamond solid) and measured T_{cat} for Ru rods (□) and spheres (O) are depicted. Reaction conditions: reaction mixture of $H_2/CO_2/N_2$ (5:1:1) at 3.5 bar pressure, 300 mg preactivated Ru catalyst, 150 °C under the illumination of 1, 5.7, or 8.5 sun light intensity.

AM 1.5 solar spectrum across the UV−vis−NIR (Figure 6c), and it clearly surpasses by manifold that of a similar catalyst that comprises only small spherical Ru nanoparticles.

Because the aspect ratio of the Ru nanorods is essential to the position of the LSPR (similar to Au nanorods) and our Ru rods are highly polydispersed, length is 153 ± 45 nm and width is 11 ± 10 nm, the broad-band character of the extinction spectrum (Figure 6a) is even more pronounced than the results obtained through optical simulations (Figure 6b). This is beneficial for harvesting sunlight and should make the photomethanation largely wavelength independent. To experimentally validate the direct connection of the impact of the broad-band absorption of our Ru catalyst on its photomethanation activity, we performed experiments at 150 °C and 1 sun light intensity in the presence of a 395 nm and of a 495 nm longpass filter. Such filters block all sunlight with wavelengths below 395 and 495 nm (SI, Figures S4 and S5), thus decreasing the overall light intensity reaching the plasmonic particles (Figure 7). Comparing the formed methane per g_{Ru} in the photomethanation with and without the use of filters, the photomethanation with longpass filters gives a lower amount of methane g_{Ru}^{-1} (Figure 7a, full spectrum: 100%; filter <395 nm: 92.3%; filter <495 nm: 82.9% all in 60 min). However, when normalizing the methane production results shown in Figure 7a with respect to the solar intensity (Figure 7b), essentially the same amount of methane per g_{Ru} per sun is formed in those three experiments (Figure 7b, values for 60 min reaction time: full spectrum, 1 sun light

intensity: 100%; filter <395 nm, 0.93 sun light intensity corrected to 1 sun light intensity: 99.3%; filter <495 nm, 0.81 sun light intensity corrected to 1 sun light intensity: 102.3%), indicating that the photomethanation is wavelength independent and thus that a broad-band sunlight absorption of the catalyst is responsible for the methanation.

Furthermore, we studied the photomethanation using Ru spheres instead of rods. The Ru spheres supported on γ-Al_2O_3 were prepared via wet immersion and direct calcination under a reducing atmosphere (Experimental Section). HAADF-STEM analysis shows that the diameter of the randomly distributed spheres is 0.88 ± 0.13 nm (Figure 8a), and through XRD analysis, we confirmed that the catalyst consists of γ-Al_2O_3 and metallic Ru (SI, S15). Since individual Ru nanospheres do not display a plasmon resonance in the solar spectrum, which was demonstrated by the calculations performed in this study for 11 nm Ru spheres, and confirmed for a broad range of sizes by other research groups,[17] the resulting catalyst powder is black and displays broad-band absorption properties between 300 and 800 nm (SI, S20). Through kinetic studies, we investigated the reaction rate obtained with this catalyst in dark and upon illumination with sunlight (1, 5.7, and 8.5 sun). Based on these results, we were able to calculate the PTM′ using the equation reported above with $k_{d'}$ obtained at the same $T_{reactor}$ instead of the same T_{cat}. For comparison, we calculated the PTM′ obtained with the rods at the same reaction conditions and with k_d obtained at the same $T_{reactor}$. The rods show significantly higher values for

PTM′, and the difference (Δ)PTM = PTM′$_{rods}$ − PTM′$_{spheres}$ is displayed in Figure 8b.

In all cases, ΔPTM is larger than zero, which demonstrated that the PTM′ is higher for rods than for spheres. Furthermore, the difference in PTM′ increases with increasing light intensity from 3.3% at 1 sun to 29.3% at 5.7 sun with similar catalyst temperatures for both spheres and rods under these conditions. At 8.5 sun, ΔPTM further increases to 41.5% and the catalyst temperature of the spheres surpasses that of the rods by 15 °C. The fact that the Ru rods are far more efficient catalysts than the Ru spheres upon solar illumination supports the hypothesis that the plasmon resonance in the UV−vis−NIR plays a crucial role in this catalytic process. For Ru spheres, this is very weak and positioned in the UV; for Ru rods, the LSPR is stronger and covers the entire solar spectrum (vide supra). Consequently, the rods are much more efficient in harvesting sunlight and using the corresponding energy to drive the photomethanation, which is a plausible explanation for the distinct difference in activity. This difference in the LSPR of Ru spheres and rods is in line with previously reported plasmonic systems.[20]

CONCLUSIONS AND OUTLOOK

We have developed and characterized a rod-shaped Ru catalyst suited for selective photoconversion of H_2 and CO_2 to CH_4 using sunlight as a sustainable energy source. Even though this Ru catalyst leads to methane production in the absence of light, upon illumination with terrestrial sunlight its activity gets significantly enhanced. At 150 °C reactor temperature and illumination with terrestrial sunlight (light intensity 1 sun), the activity is enhanced by a factor 2.1. Detailed kinetic studies clearly demonstrated that this enhancement could be fully attributed to heating of the catalyst bed upon illumination (photothermal effect). At higher light intensities of 5.7 and 8.5 sun, however, a significant nonthermal contribution was observed. This was quantified as photon-to-methane efficiencies of 22.3% (5.7 sun) and 54.8% (8.5 sun). Furthermore, we demonstrated that external heating of the reactor is not required to promote methanation when using slightly concentrated sunlight (8.5 or 10.1 sun). We attribute the sunlight-harvesting ability of the catalyst and the high photon-to-methane efficiency of the process to the UV−vis−NIR plasmonic absorption of the large, nonspherical, rodlike Ru nanoparticles present in the catalyst. For Ru spheres, with a plasmonic absorption outside of the solar spectrum in the UV-C, we observed significantly lower photon-to-methane efficiency. At 8.5 sun and 150 °C reactor temperature, the difference was 41.5%, whereas the catalyst temperature for the rods was approximately 15 °C lower than for the spheres. This insight is very valuable for the further development of plasmon catalysts for photoconversions using sunlight as an energy source. Further studies on the nature of the nonthermal contribution reported in our manuscript are currently ongoing in our laboratory. Our sunlight-fueled conversion of H_2 to methane is a promising technology to simultaneously accelerate the energy transition and reduce CO_2 emissions.

EXPERIMENTAL SECTION

Preparation of the RuO$_2$ Precatalyst (Adapted Procedure from Ref 21). A 3.2 mM Ru precursor solution was obtained by dissolving 0.104 g (0.16 mmol, 1.6 mol %) of $Ru_3(CO)_{12}$ (Aldrich, 99%) in 50 mL of tetrahydrofuran (THF) (Biosolve). The solution was stirred for approximately 2 h until all solid was dissolved. γ-Al$_2$O$_3$ (Alfa Aesar, 99%, SA 200 m^2 g^{-1}) was calcined in air at 500 °C for 6 h. Then, 1 g (9.8 mmol, 98.4 mol %) of calcined γ-Al$_2$O$_3$ was added to the precursor solution resulting in a yellow slurry. The solution was stirred for 4 h at room temperature. Subsequently, THF was removed in a rotary evaporator under reduced pressure at 45 °C. Calcination of the resulting composite powder was done in air with a heating ramp of 5 °C min^{-1} until 300 °C and at 300 °C for 2 h. After reduction, the Ru content was 6.0 wt %, as determined by inductively coupled plasma optical emission spectroscopy (ICP-OES). STEM−EDX and XRD analyses were performed to study the composition and architecture of the RuO$_2$ precatalyst (SI, S12 and S14). Surface Brunauer−Emmett−Teller area was determined to be 171 g m^{-2}.

Preactivation with H$_2$ of the Precatalyst to Form the Active Rod-Shaped Ru Catalyst. The resulting material after calcination was reduced under a hydrogen flow (10% H$_2$ in Ar, 300 mL min^{-1}) with a heating ramp of 5 °C min^{-1} until 250 °C and 250 °C for 2 h. STEM−EDX and XRD analyses were performed to study the composition and architecture of the Ru catalyst (vide supra).

Preparation of the Spherical Ru Catalyst. A 3.2 mM Ru precursor solution was obtained by dissolving 0.104 g (0.16 mmol, 1.6 mol %) of Ru$_3$(CO)$_{12}$ (Aldrich, 99%) in 50 mL of THF (Biosolve). The solution was stirred for approximately 2 h until all solid was dissolved. γ-Al$_2$O$_3$ (Alfa Aesar, 99%, SA 200 m^2 g^{-1}) was calcined in air at 500 °C for 6 h. Then, 1 g (9.8 mmol, 98.4 mol %) of calcined γ-Al$_2$O$_3$ was added to the precursor solution resulting in a yellow slurry. The solution was stirred for 4 h at room temperature. Subsequently, THF was removed in a rotary evaporator under reduced pressure at 45 °C. The resulting material was reduced under a hydrogen flow (10% H$_2$ in Ar, 300 mL min^{-1}) with a heating ramp of 5 °C min^{-1} until 250 °C and kept under hydrogen at 250 °C for 2 h. After reduction, the Ru content was 4.79 wt % determined by ICP-OES analysis. STEM−EDX and XRD analyses were performed to study the composition and architecture of the Ru catalyst.

Photomethanation Experiments. A homemade photo-reactor equipped with a solar simulator (Newport Sol3A) and reaction cell with quartz window was used for the sunlight-fueled methanation reaction (SI, S3). N$_2$ was used as an internal standard. The reactor was prepared by filling the reactor with the catalyst (300 mg) and N$_2$ and subsequent evacuation three times. Then, the reactor was filled with the reaction mixture of H$_2$ (Linde 6.0) and CO$_2$ (Linde 4.5) and diluted with N$_2$ (Linde 5.0) with the ratio H$_2$/CO$_2$/N$_2$ (5:1:1) until the total pressure was 3.5 bar (2.5 bar overpressure). Prior to each experiment, the temperature was stabilized to the desired reactor temperature in the range of 25−150 °C using electrical heating. During the experiment, the catalyst was irradiated from the top through the quartz window. The irradiation source was a solar light simulator provided with a filter of air mass coefficient 1.5 (AM 1.5), conventionally taken to 1 kW m^{-2}. Concentrated sunlight was obtained with optical elements (high flux beam concentrator, Newport 81030) up to an intensity of 10.1 sun. The moment the lamp is switched on is considered the starting time of the reaction; the CH$_4$ formation before the starting time is subtracted from the light experiments. Gas samples were taken from the reactor using a gas leak tight syringe. Gas (3 mL) was taken from the

upper part of the reactor at different times and directly measured in the gas chromatograph (compact GC Interscience). The GC is equipped with three channels, two micro thermal conductivity detectors (TCD), and one flame ionization detector (FID). The first channel, used to measure H_2, O_2, N_2, and CO, is equipped with a MolSieve 5 Å column and RT-Q bond precolumn and TCD detector. The second channel, used to measure H_2O and CO_2, is equipped with a combination of TR-U bond column and RT-Q bond column and TCD detector. The third channel, used to measure methane, ethane, and propane, is fitted with a Rtx-1, 2u column, and FID detector.

Blank experiments in the presence of the catalyst at 150 °C and illumination without CO_2 showed no reaction products, confirming that CH_4 comes from the CO_2. Also, no activity was shown when H_2 was not present in the reaction and when the catalyst was left out.

■ ASSOCIATED CONTENT

ⓢ Supporting Information

The Supporting Information is available free of charge on the ACS Publications website at DOI: 10.1021/acsomega.9b00581.

> Overview of the literature on photomethanation processes with correspondingly reported catalytic activities; images of the support, the RuO_2 precatalyst, and the rodlike Ru catalyst during synthesis; equipment for the photomethanation reactions; temperature catalyst bed; amount of CO_2, H_2, and CH_4 present during photomethanation reactions using the H_2-activated Ru catalyst at 150 °C; GC trace for a typical reaction; procedure for a typical reaction without illumination; experimental and modeling details, data, and spectra (PDF)

■ AUTHOR INFORMATION

Corresponding Author

*E-mail: pascal.buskens@tno.nl.

ORCID ⬦

Jessica Rodríguez-Fernández: 0000-0002-0609-5464

Pascal Buskens: 0000-0002-2076-2585

Author Contributions

The manuscript was written through contributions of all authors. All authors have given approval to the final version of the manuscript.

Notes

The authors declare no competing financial interest.

■ ACKNOWLEDGMENTS

■ REFERENCES

(1) Chu, S.; Cui, Y.; Liu, N. The Path towards Sustainable Energy. *Nat. Mater.* **2017**, *16*, 16−22.

(2) Brouwer, A. S.; van den Broek, M.; Seebregts, A.; Faaij, A. Impacts of Large Scale Intermittent Renewable Energy Sources on Electricity Systems, and How They Can Be Modeled. *Renewable Sustainable Energy Rev.* **2014**, *33*, 443−466.

(3) (a) Lewis, N. S.; Nocera, D. G. Powering the Planet: Chemical Challenges in Solar Energy Utilization. *Proc. Natl. Acad. Sci. U.S.A.* **2006**, *103*, 15729−15735. (b) Detz, R. J.; Reek, J. N. H.; van der Zwaan, B. C. C. The Future of Solar Fuels: When Could They Become Competitive? *Energy Environ. Sci.* **2018**, *11*, 1653−1669.

(4) Stamenkovic, V. R.; Strmcnik, D.; Lopes, P. P.; Markovic, N. M. Energy and Fuels from Electrochemical Interfaces. *Nat. Mater.* **2017**, *16*, 57−69.

(5) (a) Schüth, F. Chemical Compounds for Energy Storage. *Chem. Ing. Tech.* **2011**, *83*, 1984−1993. (b) Kondratenko, E. V.; Mul, G.; Baltrusaitis, J.; Larrazábal, G. O.; Pérez-Ramírez, J. Status and Perspectives of CO_2 Conversion into Fuels and Chemicals by Catalytic, Photocatalytic and Electrocatalytic processes. *Energy Environ. Sci.* **2013**, *6*, 3112−3135.

(6) (a) Sabatier, P.; Senderens, J. B. New Methane Synthesis. *C. R. Acad. Sci., Paris* **1902**, 134. (b) Rönsch, S.; Schneider, J.; Matthischke, S.; Schlüter, M.; Götz, M.; Lefebvre, J.; Prabhakaran, P.; Bajohr, S. Review on Methanation − from Fundamentals to Current Projects. *Fuel* **2016**, *166*, 276−296. Vogt, C.; Groeneveld, E.; Kamsma, G.; Nachtegaal, M.; Lu, L.; Kiely, C. J.; Berben, P. H.; Meirer, F.; Weckhuysen, B. M. Unravelling Structure Sensitivity in CO_2 Hydrogenation over Nickel. *Nat. Catal.* **2018**, *1*, 127−134.

(7) (a) Thampi, K. R.; Kiwi, J.; Grätzel, M. Methanation and Photo-Methanation of Carbon Dioxide at Room Temperature and Atmospheric Pressure. *Nature* **1987**, *327*, 506−508. (b) Yan, S. C.; Ouyang, S. X.; Gao, J.; Yang, M.; Feng, J. Y.; Fan, X. X.; Wan, L. J.; Li, Z. S.; Ye, J. H.; Zhou, Y.; Zou, Z. G. A Room-Temperature Reactive-Template Route to Mesoporous $ZnGa_2O_4$ with Improved Photo-catalytic Activity in Reduction of CO_2. *Angew. Chem., Int. Ed.* **2010**, *49*, 6400−6404. (c) Wang, W.-N.; An, W.-J.; Ramalingam, B.; Mukherjee, S.; Niedzwiedzki, D. M.; Gangopadhyay, S.; Biswas, P. Size and Structure Matter: Enhanced CO_2 Photoreduction by Size-Resolved Ultrafine Pt Nanoparticles on TiO_2 Single Crystals. *J. Am. Chem. Soc.* **2012**, *134*, 11276−11281. (d) Xi, G.; Ouyang, S.; Li, P.; Ye, J.; Ma, Q.; Su, N.; Bai, H.; Wang, C. Ultrathin $W_{18}O_{49}$ Nanowires with Diameters Below 1 nm: Synthesis, Near-Infrared Absorption, Photoluminescence, and Photochemical Reduction of Carbon Dioxide. *Angew. Chem., Int. Ed.* **2012**, *51*, 2395−2399. (e) Wang, Y.; Li, B.; Zhang, C.; Cui, L.; Kang, S.; Li, X.; Zhou, L. Ordered Mesoporous CeO_2-TiO_2 Composites: Highly Efficient Photocatalysts for the Reduction of CO_2 with H_2O under Simulated Solar Irradiation. *Appl. Catal., B* **2013**, *130−131*, 277−284. (f) Neațu, S.; Maciá-Agulló, J. A.; Concepción, P.; Garcia, H. Gold−Copper Nanoalloys Supported on TiO_2 as Photocatalysts for CO_2 Reduction by Water. *J. Am. Chem. Soc.* **2014**, 15969−15976. (g) Jelle, A. A.; Ghuman, K. K.; O'Brien, P. G.; Hmadeh, M.; Sandhel, A.; Perovic, D. D.; Singh, C. V.; Mims, C. A.; Ozin, G. A. Highly Efficient Ambient Temperature CO_2 Photomethanation Catalyzed by Nanostructured RuO_2 on Silicon Photonic Crystal Support. *Adv. Energy Mater.* **2018**, *8*, No. 1702277. (h) O'Brien, P. G.; Ghuman, K. K.; Jelle, A. A.; Sandhel, A.; Wood, T. E.; Loh, J. Y. Y.; Perovic, D.; Veer Singh, C.; Kherani, N. P.; Mims, C. A.; Ozin, G. A. Enhanced Photothermal Reduction of Gaseous CO_2 over Silicon Photonic Crystal Supported Ruthenium at Ambient Temperature. *Energy Environ. Sci.* **2018**, *11*, 3443−3451. (i) Yuan, L.; Lu, K.-Q.; Zhang, F.; Fu, X.; Xu, Y.-J. Unveiling the Interplay between Light-Driven CO_2 Photocatalytic Reduction and Carbonaceous Residues Decomposition: A Case Study of Bi_2WO_6-TiO_2 Binanosheets. *Appl. Catal., B* **2018**, *237*, 424−431. (j) Yuan, L.; Han, C.; Pagliaro, M.; Xu, Y.-J. Origin of Enhancing the Photocatalytic Performance of TiO_2 for Artificial Photoreduction of CO_2 through a SiO_2 Coating Strategy. *J. Phys. Chem. C* **2016**, *120*, 265−273. (k) Yuan, L.; Xu, J.-Y. Photocatalytic Conversion of CO_2 into Value-Added and Renewable Fuels. *Appl. Surf. Sci.* **2015**, *342*, 154−167. (l) Zhang, N.; Han, C.; Fu, X.; Xu, J.-Y. Function-Oriented Engineering of Metal-Based Nanohybrids for Photoredox Catalysis:

Exerting Plasmonic Effect and Beyond. *Chem* **2018**, *4*, 1832−1861. (m) Yang, M.-Q.; Cu, Y.-J. Photocatalytic Conversion of CO_2 over Graphene-Based Composites: Current Status and Future Perspective. *Nanoscale Horiz.* **2016**, *1*, 185−200.

(8) Baffou, G.; Quidant, R. Nanoplasmonics for Chemistry. *Chem. Soc. Rev.* **2014**, *43*, 3898−3907.

(9) Cole, J. R.; Halas, N. J. Optimized Plasmonic Nanoparticle Distributions for Solar Spectrum Harvesting. *Appl. Phys. Lett.* **2006**, *89*, No. 153120.

(10) Sastre, F.; Puga, A. V.; Liu, L.; Corma, A.; García, H. Complete Photocatalytic Reduction of CO_2 to Methane by H_2 under Solar Light Irradiation. *J. Am. Chem. Soc.* **2014**, *136*, 6798−6801.

(11) Meng, X.; Wang, T.; Liu, L.; Ouyang, S.; Li, P.; Hu, H.; Kako, T.; Iwai, H.; Tanaka, A.; Ye, J. Photothermal Conversion of CO_2 into CH_4 with H_2 over Group VIII Catalysts: An Alternative Approach for Solar Fuel Production. *Angew. Chem., Int. Ed.* **2014**, *53*, 11478−11482.

(12) Zhang, X.; Li, X.; Reish, M. E.; Zhang, D.; Qiang Su, N.; Gutiérrez, Y.; Moreno, F.; Yang, W.; Everitt, H. O.; Liu, J. Plasmon-Enhanced Catalysis: Distinguishing Thermal and Nonthermal Effects. *Nano Lett.* **2018**, *18*, 1714−1723.

(13) Zhang, X.; Li, X.; Zhang, D.; Su, N. Q.; Yang, W.; Everitt, H. O.; Liu, J. Product Selectivity in Plasmonic Photocatalysis for Carbon Dioxide Hydrogenation. *Nat. Commun.* **2017**, *8*, No. 14542.

(14) (a) García de Abajo, F. J.; Howie, A. Relativistic Electron Energy Loss and Electron-Induced Photon Emission in Inhomogeneous Dielectrics. *Phys. Rev. Lett.* **1998**, *80*, 5180−5183. (b) García de Abajo, F. J.; Howie, A. Retarded Field Calculation of Electron Energy Loss in Inhomogeneous Dielectrics. *Phys. Rev. B* **2002**, *65*, No. 115418. (c) Myroshnychenko, V.; Rodríguez-Fernández, J.; Pastoriza-Santos, I.; Funston, A. M.; Novo, C.; Mulvaney, P.; Liz-Marzán, L. M.; García de Abajo, F. J. Modelling the Optical Response of Gold Nanoparticles. *Chem. Soc. Rev.* **2008**, *37*, 1792−1805.

(15) (a) Shao, L.; Tao, Y.; Ruan, Q.; Wang, J.; Lin, H.-Q. Comparison of the plasmonic performances between lithographically fabricated and chemically grown gold nanorods. *Phys. Chem. Chem. Phys.* **2015**, *17*, 10861−10870. (b) Mann, D.; Nascimento-Duplat, D.; Keul, H.; Möller, M.; Verheijen, M.; Xu, M.; Urbach, H. P.; Adam, A. J. L.; Buskens, P. The Influence of Particle Size Distribution and Shell Imperfections on the Plasmon Resonance of Au and Ag Nanoshells. *Plasmonics* **2017**, *12*, 929−945.

(16) Palik, E. D.; Bennett, J. M. *Handbook of Optical Constants of Solids I and II*; Academic Press: London, San Diego, 1995.

(17) Sanz, J. M.; Ortiz, D.; Alcaraz de la Osa, R.; Saiz, J. M.; González, F.; Brown, A. S.; Losurdo, M.; Everitt, H. O.; Moreno, F. UV Plasmonic Behavior of Various Metal Nanoparticles in the Near- and Far-Field Regimes: Geometry and Substrate Effects. *J. Phys. Chem. C* **2013**, *117*, 19606−19615.

(18) (a) Rodríguez-Fernández, J.; Pérez-Juste, J.; García de Abajo, F. J.; Liz-Marzán, L. M. Seeded Growth of Submicron Au Colloids with Quadrupole Plasmon Resonance Modes. *Langmuir* **2006**, *22*, 7007−7010. (b) Payne, E. K.; Shuford, K. L.; Park, S.; Schatz, G. C.; Mirkin, C. A. Multipole Plasmon Resonances in Gold Nanorods. *J. Phys. Chem. B* **2006**, *110*, 2150−2154.

(19) Jain, P. K.; Huang, W.; El-Sayed, M. A. On the Universal Scaling Behavior of the Distance Decay of Plasmon Coupling in Metal Nanoparticle Pairs: A Plasmon Ruler Equation. *Nano Lett.* **2007**, *7*, 2080−2088.

(20) Zhang, X.; Chen, Y. L.; Liu, R.-S.; Tsai, D. P. Plasmonic Photocatalysis. *Rep. Prog. Phys.* **2013**, *76*, No. 046401.

(21) Kim, T. W.; Oh, J.; Suh, Y.-W. Hydrogenation of 2-Benzylpyridine over Alumina-Supported Ru Catalysts: Use of $Ru_3(CO)_{12}$ as a Ru Precursor. *Appl. Catal., A* **2017**, *547*, 183−190.